Research Article | Vol. 25, No. 22 | 30 Oct 2017 | OPTICS EXPRESS 27678
Optics EXPRESS

Silicon nitride waveguide platform for fluorescence microscopy of living cells

JEAN-CLAUDE TINGUELY,[1,2] ØYSTEIN IVAR HELLE,[1,2] AND BALPREET SINGH AHLUWALIA[1,*]

[1]*Department of Physics and Technology, UiT-The Arctic University of Norway, 9037 Tromsø, Norway*
[2]*Authors with equal contribution to the paper*
**balpreet.singh.ahluwalia@uit.no*

Abstract: Waveguide chip-based microscopy reduces the complexity of total internal reflection fluorescence (TIRF) microscopy, and adds features like large field of view illumination, decoupling of illumination and collection path and easy multimodal imaging. However, for the technique to become widespread there is a need of low-loss and affordable waveguides made of high-refractive index material. Here, we develop and report a low-loss silicon nitride (Si_3N_4) waveguide platform for multi-color TIRF microscopy. Single mode conditions at visible wavelengths (488-660 nm) were achieved using shallow rib geometry. To generate uniform excitation over appropriate dimensions waveguide bends were used to filter-out higher modes followed by adiabatic tapering. Si_3N_4 material is finally shown to be biocompatible for growing and imaging living cells.

OCIS codes: (180.4243) Near-field microscopy; (130.0130) Integrated optics; (180.2520) Fluorescence microscopy; (170.3880) Medical and biological imaging.

References and links

1. A. Dhakal, P. Wuytens, F. Peyskens, A. Z. Subramanian, N. Le Thomas, and R. Baets, "Silicon-nitride waveguides for on-chip Raman spectroscopy," Proc. SPIE **9141**, 91410 (2014).
2. G. Yurtsever, P. Dumon, W. Bogaerts, and R. Baets, "Integrated photonic circuit in silicon on insulator for Fourier domain optical coherence tomography," Proc. SPIE **7554**, 75514B (2010).
3. F. T. Dullo, S. Lindecrantz, J. Jágerská, J. H. Hansen, M. Engqvist, S. A. Solbø, and O. G. Hellesø, "Sensitive on-chip methane detection with a cryptophane-A cladded Mach-Zehnder interferometer," Opt. Express **23**(24), 31564–31573 (2015).
4. P. Muellner, E. Melnik, G. Koppitsch, J. Kraft, F. Schrank, and R. Hainberger, "CMOS-compatible Si3N4 waveguides for optical biosensing," Procedia Eng. **120**, 578–581 (2015).
5. A. Gorin, A. Jaouad, E. Grondin, V. Aimez, and P. Charette, "Fabrication of silicon nitride waveguides for visible-light using PECVD: a study of the effect of plasma frequency on optical properties," Opt. Express **16**(18), 13509–13516 (2008).
6. A. Z. Subramanian, P. Neutens, A. Dhakal, R. Jansen, T. Claes, X. Rottenberg, F. Peyskens, S. Selvaraja, P. Helin, B. Du Bois, K. Leyssens, S. Severi, P. Deshpande, R. Baets, and P. Van Dorpe, "Low-Loss Singlemode PECVD Silicon Nitride Photonic Wire Waveguides for 532-900 nm Wavelength Window Fabricated Within a CMOS Pilot Line," IEEE Photonics J. **5**, 220809 (2013).
7. D. J. Moss, R. Morandotti, A. L. Gaeta, and M. Lipson, "New CMOS-compatible platforms based on silicon nitride and Hydex for nonlinear optics," Nat. Photonics **7**, 597–607 (2013).
8. J. Riemensberger, K. Hartinger, T. Herr, V. Brasch, R. Holzwarth, and T. J. Kippenberg, "Dispersion engineering of thick high-Q silicon nitride ring-resonators via atomic layer deposition," Opt. Express **20**(25), 27661–27669 (2012).
9. W. Zeru, C. Yujie, Z. Tianyou, S. Zengkai, W. Yuanhui, X. Pengfei, Z. Yanfeng, and Y. Siyuan, "Design and optimization of optical modulators based on graphene-on-silicon nitride microring resonators," J. Opt. **19**, 045801 (2017).
10. A. Z. Subramanian, E. Ryckeboer, A. Dhakal, F. Peyskens, A. Malik, B. Kuyken, H. L. Zhao, S. Pathak, A. Ruocco, A. De Groote, P. Wuytens, D. Martens, F. Leo, W. Q. Xie, U. D. Dave, M. Muneeb, P. Van Dorpe, J. Van Campenhout, W. Bogaerts, P. Bienstman, N. Le Thomas, D. Van Thourhout, Z. Hens, G. Roelkens, and R. Baets, "Silicon and silicon nitride photonic circuits for spectroscopic sensing on-a-chip," Photon. Res. **3**, B47–B59 (2015).
11. F. T. Dullo and O. G. Hellesø, "On-chip phase measurement for microparticles trapped on a waveguide," Lab Chip **15**(19), 3918–3924 (2015).
12. B. Agnarsson, S. Ingthorsson, T. Gudjonsson, and K. Leosson, "Evanescent-wave fluorescence microscopy using symmetric planar waveguides," Opt. Express **17**(7), 5075–5082 (2009).

#303400 https://doi.org/10.1364/OE.25.027678
Journal © 2017 Received 21 Aug 2017; revised 21 Sep 2017; accepted 29 Sep 2017; published 25 Oct 2017

Optics EXPRESS

13. B. Agnarsson, A. B. Jonsdottir, N. B. Arnfinnsdottir, and K. Leosson, "On-chip modulation of evanescent illumination and live-cell imaging with polymer waveguides," Opt. Express **19**(23), 22929–22935 (2011).
14. H. M. Grandin, B. Städler, M. Textor, and J. Vörös, "Waveguide excitation fluorescence microscopy: A new tool for sensing and imaging the biointerface," Biosens. Bioelectron. **21**(8), 1476–1482 (2006).
15. A. Hassanzadeh, M. Nitsche, S. Mittler, S. Armstrong, J. Dixon, and U. Langbein, "Waveguide evanescent field fluorescence microscopy: Thin film fluorescence intensities and its application in cell biology," Appl. Phys. Lett. **92**, 233503 (2008).
16. B. Agnarsson, A. Lundgren, A. Gunnarsson, M. Rabe, A. Kunze, M. Mapar, L. Simonsson, M. Bally, V. P. Zhdanov, and F. Höök, "Evanescent Light-Scattering Microscopy for Label-Free Interfacial Imaging: From Single Sub-100 nm Vesicles to Live Cells," ACS Nano **9**(12), 11849–11862 (2015).
17. M. J. Levene, J. Korlach, S. W. Turner, M. Foquet, H. G. Craighead, and W. W. Webb, "Zero-mode waveguides for single-molecule analysis at high concentrations," Science **299**(5607), 682–686 (2003).
18. R. Diekmann, O. I. Helle, C. I. Oie, P. McCourt, T. R. Huser, M. Schuttpelz, and B. S. Ahluwalia, "Chip-based wide field-of-view nanoscopy," Nat Photonics **11**, 322 (2017).
19. F. T. Dullo, J. C. Tinguely, S. A. Solbo, and O. G. Helleso, "Single-Mode Limit and Bending Losses for Shallow Rib Si3N4 Waveguides," IEEE Photonics J. **7**, 1–11 (2015).
20. H. R. Philipp, "Optical Properties of Silicon-Nitride," J. Electrochem. Soc. **120**, 295–300 (1973).
21. C. Guo, M. Kong, W. Gao, and B. Li, "Simultaneous determination of optical constants, thickness, and surface roughness of thin film from spectrophotometric measurements," Opt. Lett. **38**(1), 40–42 (2013).
22. D. F. G. Gallagher and T. P. Felici, "Eigenmode expansion methods for simulation of optical propagation in photonics - Pros and cons," Integrated Optics: Devices, Materials, and Technologies VII **4987**, 69–82 (2003).
23. Y. Fu, T. Ye, W. Tang, and T. Chu, "Efficient adiabatic silicon-on-insulator waveguide taper," Photon. Res. **2**, A41–A44 (2014).
24. F. Prieto, B. Sepulveda, A. Calle, A. Llobera, C. Domínguez, A. Abad, A. Montoya, and L. M. Lechuga, "An integrated optical interferometric nanodevice based on silicon technology for biosensor applications," Nanotechnology **14**, 907 (2003).
25. C. E. Aitken, R. A. Marshall, and J. D. Puglisi, "An oxygen scavenging system for improvement of dye stability in single-molecule fluorescence experiments," Biophys. J. **94**(5), 1826–1835 (2008).

1. Introduction

Photonics integrated circuits (PICs) based on high refractive index contrast (HIC) between the core and the cladding has attracted significant research attention during the last decade [1–10]. The HIC enables tight confinement of the light inside the waveguide, enabling ultra-compact waveguide structures with small bend radii. These properties of HIC are used to fabricate high-density PICs and integrated optical functions such as optical modulators, switches, and arrayed waveguides with a small footprint. Spiral waveguide geometries in HIC waveguides are used to significantly increase the interaction length between the sample and the evanescent field of the waveguide [1] opening opportunities to develop, e.g., on-chip Raman spectroscopy [1] and on-chip optical coherence tomography (OCT) [2]. In addition, by fabricating HIC waveguides with a core thickness of 100-200 nm, the intensity of the evanescent field can be greatly increased. Consequently, HIC waveguide platforms provide high sensitivity when used for optical sensors (chemical, gas and biological) [3, 4]

Different materials have been explored to fabricate HIC waveguide platforms. For infrared wavelengths, silicon waveguides (n = 3.5) using silicon-on-insulator technology are commonly used. For the visible regime, materials such as tantalum pentoxide (Ta_2O_5), titanium pentoxide (TiO_2) and silicon nitride (Si_3N_4) have been utilized. Among the explored HIC materials within visible wavelengths, Si_3N_4 has attracted the maximum attention due to its suitable material properties and the compatibility of Si_3N_4 fabrication process with standard CMOS fabrication line. The suitable material property includes transparency in visible wavelength, low absorption and high refractive index contrast. Exhibiting a refractive index of around 2 at the visible regime, the HIC with the substrate/cladding (typically SiO_2, n = 1.46) enables integrated functions with a small footprint, which is not possible with materials exhibiting lower refractive index contrasts. Various applications have been developed both in linear [4, 6] and non-linear optics [7] using Si_3N_4 platform. The Si_3N_4 waveguide has been employed to develop different integrated optical functions such as ring resonators [8], modulators [9], switches [9], sensors [3], spectroscopy [10] and waveguide trapping [11]. Being transparent with low auto-fluorescence and low absorption in the visible range further makes Si_3N_4 compatible with fluorescence techniques for bio-imaging. In

Optics EXPRESS

addition, the compatibility of Si_3N_4 with standard CMOS fabrication lines is able to deliver high volume production of photonic chips, decreasing production costs. Low-loss Si_3N_4 waveguide platforms have been reported using CMOS fabrication compatible process [4–6] and the foundry services for Si_3N_4 platforms became commercially available in recent years.

In this work, we report the usage of Si_3N_4 waveguide platform for integrated optical microscopy for live cell imaging applications. The previous reports [12–18] on integrated optical microscopy employed different core materials including both high and low refractive index contrast materials. Si_3N_4 platform has not been explored for fluorescence microscopy of living cells. As Si_3N_4 is turning out to be a preferred HIC material at visible wavelengths, a systematic investigation of the suitability of Si_3N_4 waveguide platforms for bio-imaging applications is beneficial. In this paper we designed, fabricated and characterized Si_3N_4 rib waveguides to possess single mode behaviour at visible wavelengths that are used in fluorescence imaging (488-660 nm). We also simulated the bend loss and adiabatic tapering length of shallow Si_3N_4 rib waveguides (2-8 nm rib height) for visible wavelengths. The simulation parameters are compared to experimental measurements. Finally, the low-loss Si_3N_4 waveguide platform is shown to be biocompatible with the imaging of living cells.

2. Si_3N_4 waveguide platform for TIRF microscopy

High-specificity, high-resolution and live-cell compatibility made fluorescence microscopy a vital tool in modern bio-medical imaging and diagnosis. The fluorophores specifically bind to the biological target providing high-contrast imaging of the intra-cellular structures with low background. To further reduce the background signal, total internal reflection fluorescence (TIRF) microscopy can be used. Contrary to epi-fluorescence where the entire cell is illuminated, TIRF microscopy exposes only a thin section of the cells through the evanescent field. As the evanescent field decays exponentially at the interface, only a thin, typically 100-200nm section away from the surface is illuminated. Consequently, TIRF microscopy provides a high signal-to-noise ratio by reducing the background signal. TIRF microscopy has found applications for imaging targets in close proximity to the cell membrane, such as cell membrane trafficking and focal adhesion points.

The evanescent field is commonly generated using a specialized high numerical aperture (N.A.) and high magnification TIRF objective lens. By this method, the dimension of the illuminated region is given by the magnification of the objective lens, which also collects the emitted fluorescence. This limits the field-of-view down to around 100 x 100 μm^2. Another way of setting up an evanescent field for TIRF microscopy is by using optical waveguides [12, 14, 15, 17,18]. In waveguide chip-based microscopy, the illumination and collection light paths are efficiently decoupled, opening several opportunities for bio-imaging. As the evanescent field is generated along the entire length of the waveguide, a low magnification objective lens can be employed to acquire TIRF images over a large field-of-view of even millimetre range [18]. Waveguide-based TIRF exhibits thus many advantages compared to conventional TIRF systems, such as a compact and user-friendly set-up (e.g. in-coupling can be provided by optical fiber), low cost as mass produced chips circumvent the expensive TIRF lens, the aforementioned flexibility at the collection path for large field of view imaging, and easy multi-color TIRF imaging at multiple wavelengths without additional optical alignment and mechanical adjustments.

Recently it was shown that the light intensities generated by the waveguide chip made of HIC material enable blinking of single molecules for super-resolution microscopy techniques [18]. The high intensity in the evanescent field was generated by fabricating thin waveguides (150 nm in thickness) made of high refractive index contrast (HIC) material such as Si_3N_4. A Si_3N_4 waveguide chip was used to demonstrate two different optical nanoscopy techniques, one based on *d*STORM (direct stochastic optical reconstruction microscopy) and another based on ESI (entropy-based super-resolution imaging). Waveguide chip-based nanoscopy displayed an optical resolution of 47 nm using a 60x/1.2NA objective, and by simply

Optics EXPRESS

changing the collection objective lens to 20x, super-resolution imaging (with a resolution of 139 nm) was obtained over an extra-ordinary large f-o-v of 0.5 x 0.5 mm^2 [18]. Multi-color waveguide chip-based *d*STORM visualized the connection of the actin cytoskeleton and plasma membrane fenestrations on liver sinusoidal endothelial cells. As compared to chip-based *d*STORM, chip-based ESI provides higher temporal resolution but lower spatial resolution. Waveguide based ESI was performed by modulating multi-mode interference (MMI) patterns of the guided light within the waveguide..MMI are typically known as an issue at waveguide-based illumination, especially when using waveguides with dimensions to accommodate cells (10-50 μm wide). The interference pattern provides then an uneven illumination of the surface with dark regions within the imaging field. A reduction in the effect of the MMI patterns was demonstrated by subsequently exciting sub-sets of modes by scanning the input coupling objective along the input facet of wide waveguides, and then averaging the mode patterns out [18]. A drawback of this approach, in addition to the need for delicate equipment for mode averaging, is the obvious reduction in temporal resolution associated with the mode averaging procedure, limiting the technique to fixed cells. Here, we show a different approach to achieve single mode (and thus uniform) illumination, by using both waveguide bends to filter out higher order modes and then adiabatically tapering of single mode waveguides up to dimensions suitable for fluorescence imaging. This strategy further strengthens advantages of waveguide-TIRF previously mentioned in this section.

2.1 Simulations

Simulations were performed to optimize the waveguide parameters such that uniformity and high intensity in the evanescent field is obtained. In fluorescence microscopy, laser lines spanning the whole visible spectrum are commonly used. We based the waveguide simulations on the most typical excitation wavelengths 488 nm, 561 nm and 660 nm. In order to achieve uniform illumination, the waveguide geometry was optimized to guide only the fundamental mode at the wavelengths of interest. The HIC of Si_3N_4 together with the requirement of visible wavelengths puts stringent conditions on the waveguide geometry to achieve the single mode condition. Compared to slab waveguides, challenged waveguide geometries (strip and rib) provide higher intensity in the evanescent field. Figure 1(a) shows the schematic diagram of a strip and rib waveguide. For the strip geometry, the single mode condition for Si_3N_4 is achieved with a sub-micron wide waveguide [6], which would require the need of projection exposure systems as steppers, electron-beam lithography or deep-UV lithography. However, the rib geometry should maintain single mode behaviour for wider waveguide geometry, e.g., 1-1.5 μm, making the fabrication process feasible with conventional photolithography and thus less demanding. Moreover, as cells are 10-25 μm in size, it is preferred to fabricate wide waveguides (>25 μm) with single mode condition. A single mode rib waveguide is therefore adiabatically tapered to provide uniform excitation over large areas. Two different designs are proposed (design A and B, as depicted in Fig. 1(b), one being a straight geometry (A) and the other including a bend section (B). As higher order modes have much higher bend losses, bend section was used to filter out higher order modes and thus ensuring single mode condition.

Simulations to determine the single mode geometry were performed using the film mode-matching (FMM) solver of the commercial software Fimmwave (Photon Design, UK). The FMM solver, a numerical technique, divides a waveguide geometry into vertical slices which are uniform laterally but multi-layered vertically. A 2D model is then composed of the Maxwell solutions found for the 1D TE (transverse electric) and TM (transverse magnetic) polarization modes of each vertical slice, with the mode amplitude obtained through the continuity of the tangential fields at the slice interface and boundary conditions. By using the FMM solver, single mode conditions were determined by calculating the largest rib height for a given width and slab height where no solution for the first-order mode could be found. As the single mode condition geometry is polarization dependent, the results differ depending on

Optics EXPRESS

the electric field's orientation. TM modes of shallow rib waveguides exhibit a hybrid polarization character with the strength of the resulting minority fields varying with geometry. Approximations to this character mostly result in erroneous results. This work will only discuss results for transverse electric (TE) modes, which do not present such behaviour. Leakage losses of TM modes and their influence on, e.g., bending losses have been discussed previously [19].

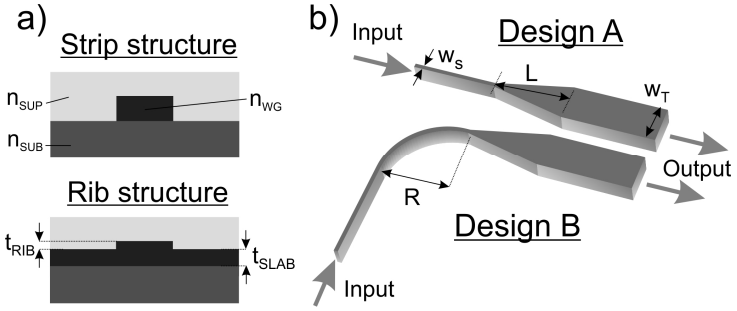

Fig. 1. a) Cross-section scheme of strip vs. rib waveguide geometry. n_{SUP}, n_{WG}, n_{SUB}: refractive indexes of superstrate, guiding material and substrate, respectively. t_{RIB}, t_{SLAB}: thicknesses of rib and slab regions. b) Top view scheme of waveguide designs demonstrating tapering of the waveguide width (design A and B) and bend structure (design B). w_S: start width, w_T: tapered width, L: taper length, R: bend radius.

As start parameters, a waveguide width of 1.5 µm was taken as a lower reproducible limit of the contact photolithography process, avoiding the more demanding scanning/stepping or e-beam processing techniques. Simulations suggested that a Si_3N_4 thickness of 150 nm (rib and slab thickness, $t_{RIB} + t_{SLAB}$) leads to an evanescent field of around 150 nm penetration depth. The curves in Fig. 2(a) display the results for single mode condition calculations for waveguides with a SiO_2 cladding at 488 nm, 561 nm and 660 nm. Refractive indexes taken for Si_3N_4 were 2.037, 2.021 and 2.007 [20], and for SiO_2 1.482, 1.479 and 1.475 at 488 nm, 561 nm and 660 nm, respectively [21]. Single mode condition simulations in Fig. 2(a) display that as the total thickness of the waveguide decreases, a smaller rib height t_{RIB} is required to keep the single mode condition. Intuitively, the rib height to maintain the single mode condition will also decrease with decreasing wavelengths. A core thickness ($t_{RIB} + t_{SLAB}$) of 150 nm was chosen for the fabrication. The simulation results indicate that for this total thickness of 150 nm, a rib height of 4 nm (t_{RIB}) and slab height of 146 nm (t_{SLAB}) would provide single mode condition for a 1.5µm wide, SiO_2 cladded waveguide at the three considered wavelengths. These dimensions will be taken into consideration for the rest of this work.

Adiabatic taper length

After simulating the parameters for single mode condition for a 1.5 µm wide waveguide, further simulations were carried to determine the adiabatic tapering length. An increase in the width of the waveguide will typically enable higher order modes to be guided. By tapering the waveguide slowly and adiabatically, the guidance of only the fundamental mode is preserved. The adiabaticity is a function of the initial and the final waveguide widths (w_S and w_T), the taper length (L), and the taper shape, as schematically represented in Fig. 1(b). The commercial software Fimmprop^{TM}, a 3D modelling expansion to the Fimmwave software, was used for the taper simulations. Fimmprop^{TM} is based on the EigenMode Expansion Method, a fully vectorial, bi-directional algorithm where the main approximation is the chosen number of propagating and radiation modes for a given geometry [22]. The adiabaticity parameter shown in Figs. 2(b) and 2(c) is defined as the percentage of the guided light present at the zero-order mode. A tapered single mode waveguide requires adiabaticity values close to 100%. The adiabaticity was determined by computing a number of modes

Optics EXPRESS

accepted at the end width of the waveguide and analysing the power distribution among them according to a taper length L. The taper profile can assume different shapes, e.g., linear, exponential or Gaussian. A linear shape was chosen based on published literature [23] pointing towards a better efficiency compared to the Gaussian and exponential shapes and better stability compared to the parabolic shapes. Convergence tests were performed for the considered number of modes. Figure 2(b) displays the results for the three different end widths at 660 nm. Results suggest 99% adiabacity from a start width w_S = 1.5 µm to an end width w_T = 12.5 µm with a taper length around L = 500 µm. The same efficiency for the end width w_T = 25 µm was achieved with the taper length L = 2000 µm and a taper length of over 4000 µm was required for the end width w_T = 50 µm. In order to undergo a compromise with the propagation losses and the structure size, the taper parameters for the experiments were set as w_T = 25 µm and L = 2000 µm. Figure 2(c) displays the minor difference in the taper efficiency for the three utilized wavelengths (over 98% for all wavelengths at L = 2000 µm) at the set parameters.

Bend losses

A Fimmprop model was used to estimate bend losses for a rib waveguide as a function of the bend radius (R). The model first considers a lossless straight section, which is then bent 90°. The power loss is estimated at the structure's output. Figure 2(d) displays the simulation results, where a significant difference in the bend losses between the three wavelengths is evident. For a bend radius of R = 2000 µm, the bend losses are below 1 dB at 561 nm and 488 nm while being around 3.5 dB at 660 nm. Transition losses are also strongest at longer wavelengths, with a model at 660 nm estimating them to be less than 0.1dB at R = 3000 µm and below 0.25dB at R = 500 µm.

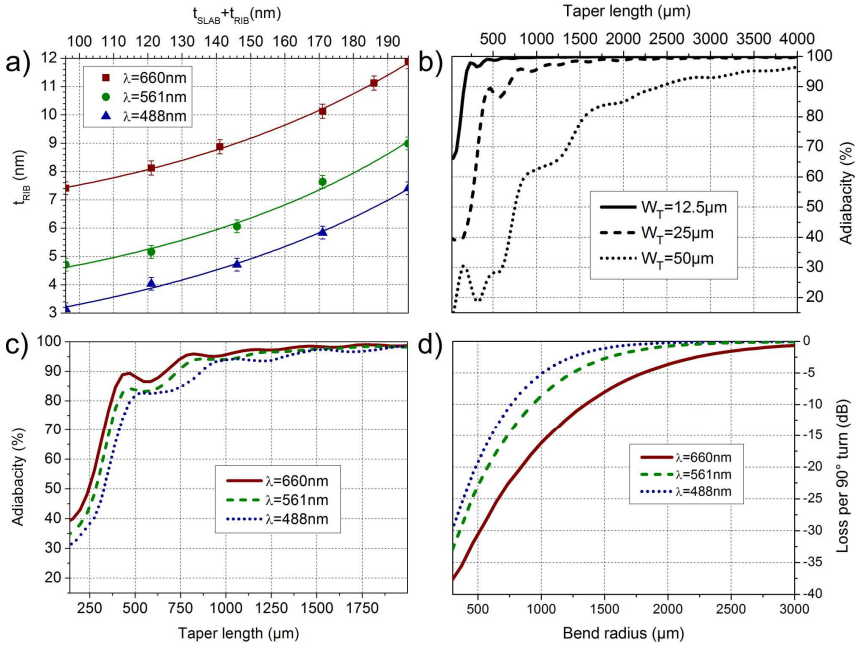

Fig. 2. a) Single mode condition simulations for TE polarized modes, 1.5µm rib width, 1.5µm SiO_2 cladding. Single mode behaviour expected below the fitted line for the given wavelength and geometry. b) Taper adiabaticity simulation, w_S = 1.5 µm to different end widths, λ = 660nm. c) Taper adiabaticity simulations, w_S = 1.5 µm to w_T = 25 µm. d) Simulation of power loss after a 90° bend as a function of bend radius.

Optics EXPRESS

2.2 Fabrication and characterization of the waveguides

Fabrication

Waveguide chips were produced at the Institute of Microelectronics Barcelona (IMB-CNM, Spain). Silica layer with a thickness of 2 µm was first grown thermally on a silicon chip, followed by the deposition of Si_3N_4 layer using low-pressure chemical vapor deposition (LPCVD) at 800°C. Standard photolithography was employed to define the waveguide geometry using photoresist, and reactive ion etching (RIE) used to fabricate a waveguide rib of given height. The remaining photoresist was removed, and finally a 1.5-2 µm thick top cladding layer deposited by plasma-enhanced chemical vapor deposition (PECVD) at 300°C. To seed the cells at specific imaging areas, the top cladding was removed using RIE and wet etching. The details of the fabrication optimization and process can be found elsewhere [24]. ·All waveguides were fabricated with a total Si_3N_4 thickness of 150 nm and 4 nm rib height. The initial width of the waveguide was 1.5 µm, later adiabatically tapered out to 25 µm. The bend radius was set to 2 mm.

Characterization

The manufactured parameters were characterized using scanning electron microscopy and a surface profiler. The surface profiler measurements verified an average rib height of 4.0 nm within the noise level of the system (0.6 nm). Scanning electron microscopy measurements indicated a possible variation of ± 0.1 µm over the specified 1.5 µm wide width.

Single mode conditions

Optical waveguides of 1.5µm width were characterized for single mode behaviour at the three wavelengths considered for the simulations. When the fundamental mode is excited in a waveguide, the resulting scattered light will appear homogenous and stationary for all possible coupling positions. If higher order modes are present, multi-mode interference (MMI) can be observed, and the scattered light along the waveguide will be modulated. To investigate this, the input coupling objective lens was scanned along the width of the waveguide using a piezo translation stage and image sequences of the scattered light were captured using an upright microscope. The experimental set-up is shown in Fig. 3. For waveguides only supporting the fundamental mode, only a straight pattern can be observed (Visualization 1). For waveguides that support higher order modes, MMI as an undulated pattern is visible (Visualization 2). Figures 4(a) to 4(c) shows scattered light from a waveguide designed for 1.5 µm width at three different wavelengths. These geometries indicate single mode behaviour at λ = 660 nm, while λ = 561nm and λ = 488 nm appear to be supporting higher order modes. This is particularly visible at λ = 488 nm, Fig. 4(c), where the undulation pattern in the guided light can be observed. Despite being in disagreement with the simulation results, the multimode behaviour at shorter wavelengths might be explained due to slight variation in the parameters of the fabricated waveguides (width and effective refractive index).

Waveguides were adiabatically tapered using both designs A and B as represented in Fig. 1(b) (w_S = 1.5 µm, w_T = 25 µm, L = 2 mm, R = 2 mm). The tapered waveguides following design A, Figs. 4(d)-4(f), and design B, Figs. 4(g)-4(i), were inspected for single mode condition at the three wavelengths. Figure 4(d) shows that 25 µm wide waveguide is still single moded at λ = 660 nm as the scattered light appears uniform. However, at λ = 561nm, Fig. 4(e), a dark band caused by multi-mode interference is visible in the scattered image. As expected, Fig. 4(f) shows that decrease of the wavelength to 488 nm results in even stronger MMI patterns.

Optics EXPRESS

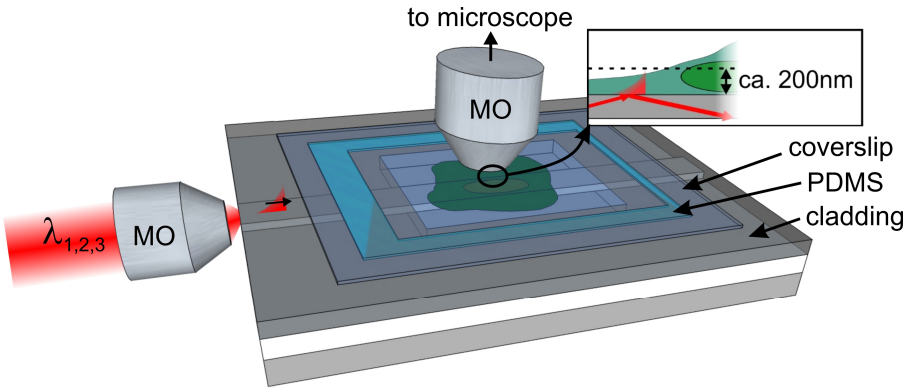

Fig. 3. Schematic diagram of the experimental setup. Imaging area at cladding is opening allowing for specimen contact to waveguide surface. Inset: approximate penetration depth of evanescent field. λ_1, λ_2, λ_3: guiding/excitation wavelengths, MO: microscope objective.

Higher order modes have several orders of magnitude higher bend losses as compared to the fundamental mode. This can be taken advantage of to filter out guided higher order modes by adding bend sections as schematized in Fig. 1(b), design B. Structures were designed where a straight 1.5 µm wide waveguide was first bend (R = 2 mm) and then tapered to 25 µm. While Visualization 3 exhibits the scattered light from a 488 nm laser in the straight 1.5 µm wide waveguide where multimode interference is clearly visible, Visualization 4 shows scattered light from the same waveguide after a bend with 2 mm radius suggesting single mode behaviour. Figures 4(g)-4(i) depict the scattered light from a 25 µm wide waveguide having the taper after a bend with a radius of 2 mm for the three different wavelengths. Comparing Figs. 4(e)-4(f) to Figs. 4(h)-4(i), it is evident that the previously observed interference patterns are removed by the bend structures (i.e by design B).

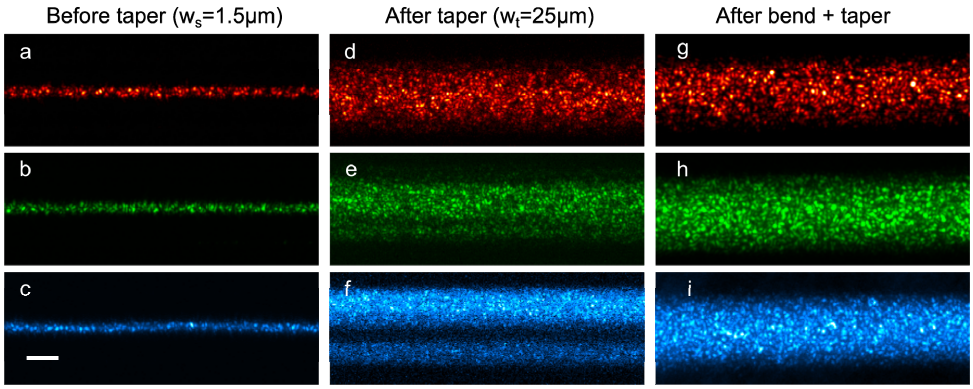

Fig. 4. Optical image of the scattered light from a waveguide at three wavelengths, (a, d, g): 660nm; (b, e, h): 561 nm and (c, f, i): 488 nm. a) to c) straight 1.5 µm wide waveguide. Multimode behaviour is observed for b) and c). d) to f): Adiabatic tapering to 25 µm width observed at d) while multimode behaviour was carried on at e) and f). g) to i): Bend section with 2mm radius preceding the taper structure removing multimode interference. Scalebar: 5 µm. Associated Visualization 1, Visualization 2, Visualization 3, and Visualization 4.

Loss measurement

The propagation losses of the waveguide for three wavelengths were measured using scattering analysis. Images of scattering from guided light were captured with subsequent translation of an upright microscope and post-processed to remove saturated pixels. Saturated pixels originate from strongly scattered light representing fabrication imperfections. An average value for each scattered image was used to track the decaying intensity of the

Optics EXPRESS

propagating light as a function of the waveguide length. The result was plotted on a log-scale with the linear fit decay as the estimate for the propagation loss. Four different measurements for each wavelength and polarization state were performed for waveguides with lengths between 1 and 2 cm, the weighted averages being shown in Table 1. The propagation loss of the Si_3N_4 was less than 1 dB/cm at 660 nm wavelength (both polarizations) and still reasonably low at 561 nm (2-2.5 dB/cm). However, the propagation loss at 488 nm was very high for both polarizations (10 dB/cm). It is very likely that the high loss at shorter wavelengths (i.e. 488 nm) is related to material absorption, visible as autofluorescence. The autofluorescence has a similar exponential increase of its intensity if moving from 660 nm to 488 nm.

Table 1. Propagation loss for 1.5 µm wide Si_3N_4 waveguides. Single values averaged from four different waveguides. The measurement uncertainty is estimated to one digit.

	TM	TE
488 nm	10.5	10.2
561 nm	1.9	2.6
660 nm	0.7	0.5

Bend losses were measured by comparing the intensity at the output facet of different waveguides. To minimize systematic errors, only waveguides on the same chip were compared. The structures contain both straight waveguides (no bends) and bend designs of different radii as shown in Fig. 5(a). The bend designs were shaped as a composite of two + 60° and two −60° curvatures. The straight waveguide acts as a reference for comparing the bend losses associated with the different bend radii, assuming the excess loss measured from the bending itself and the extra propagation loss associated with the extra arc-length of the bend sections. The output light was coupled out of the waveguides and captured by a 20x NA0.4 objective lens. An iris was placed at the objective focal point to filter out any unguided light, and finally the light was directed to an optical power meter. Figure 5(a) plots the simulated and the measured bend losses for the bend geometries in Fig. 5(b). For a bend radius of 2 mm at 561 nm and 660 nm wavelengths, the bend losses measured experimentally were similar to the values predicted by the simulation. Discrepancies on the measured and the simulated bend losses were obtained for the short bend radius, i.e. (500 µm) at all wavelengths. For a rib waveguide, the Si_3N_4 slab beneath can still guide light leaking out from the waveguide. For shallow rib waveguides as used in this work, part of the light leaking out at the sharp bends (e.g. 500 µm) is being guided by the slab beneath and eventually re-coupled onto the straight section after the bend. This effect was prominent for sharp bends and also at 488 nm wavelength, thus accounting for the higher discrepancies at 488 nm.

Optics EXPRESS

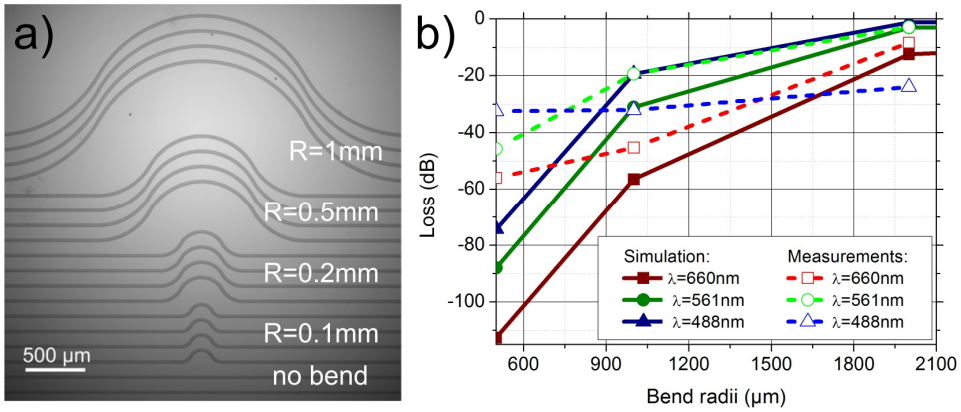

Fig. 5. a) Waveguide design for measurement of bend losses. Microscope image shows the different waveguide test structures with no bend and increasing bend radii. b) Measurements vs. simulations for a bend loss structure as represented in a).

3. Chip based fluorescence imaging of fixed and live cells

3.1 Experimental set-up

The setup was built around a modular upright microscope from Olympus (BXFM), see Fig. 3. The microscope body was mounted on two linear motorized translation stages, providing freedom to move the microscope. The waveguide chip was held by a vacuum chuck mounted on a multi-axis flexure stage (Thorlabs, RBL 13D). Light from three lasers sources (660 nm Cobolt Flamenco, 561 nm Cobolt Jive and 488 nm Oxxious LBX 488) was combined and coupled into the waveguide chip. The laser beams were individually expanded and collimated to fit the back aperture of the coupling objective lens (Olympus NPlan 50x NA0.5), which focussed the light onto the input facet of the waveguide. The coupling objective lens was mounted on a piezo stage (Melles Griot, NanoMax-HS) to allow for fine-tuning of the input coupling. The light coupled into the waveguide is guided to the imaging region. The cladding on the imaging area was removed to allow the specimen to come in direct contact with the waveguide surface and thus the evanescent field. The fluorescence is excited by the evanescent field and the emitted signal is captured by a high N.A. objective lens (Olympus 60x NA1.2) and filtered through lowpass (AHF660, AHF561, Edmund 488) and bandpass filters before the signal is imaged onto a sCMOS camera (Hamamatsu Orca flash v3). Post processing of the image data was done using the open source software ImageJ.

3.2 Sample preparation

Waveguide chips were fitted with a custom made micro-chamber to host cells and aqueous image buffer. The micro-chambers were fabricated using polydimethylsiloxane (PDMS) which was spin coated on the bottom of a petri dish to achieve an approximately 130 µm thick homogeneous layer. After curing, the micro-chambers were cut to size with a scalpel and placed on the chip using a tweezer. PDMS will adhere to both the waveguide and cover glass coming on top of it, creating a hermetic chamber.

Human Merkel carcinoma cells (MCC13) were seeded directly on the waveguide surface and left to grow for 48 hours inside an incubator. The cells were fixed using 4% paraformaldehyde (PFA) for 10 minutes at room temperature (RT). Cell membrane permeabilization was performed using 0.1% Trition X-100 at RT. To reduce unspecific binding of fluorophores on the waveguide surface, the chip was incubated with 5% bovine serum albumin (BSA) for 20 minutes at RT. The microtubules network was stained for 45 minutes with Alexa488 a-tubulin (Termofisher, #MA138000A488) at a concentration of 1/400 in 5% BSA at RT. The plasma membrane was stained for 20 minutes at RT using

Optics EXPRESS

CellMask deep red (Termofisher, #C10046) (CMDR), the stock solution diluted to 1/1000 in phosphate buffered saline (PBS). Each step in this protocol was followed by three gentle rinsing steps using PBS buffer. The PBS-based imaging media contained an enzymatic oxygen scavenging system [25] to reduce photobleaching of the fluorophores.For live cell imaging, human trophoblast cells (HTR-8) were grown on the waveguide inside an incubator for 48 hours. The plasma membrane was stained using CellMask green (Termofisher, #H32714) at a concentration of 1/1000 in PBS for 20 minutes. The chip was gently washed with live cell buffer media (Termofisher, #21875091). The chambers were filled with live cell imaging buffer (Termofisher, #A14291DJ) and imaged within 30 minutes after staining.

3.3 Imaging of fixed and live cells

The tapered waveguide (25 μm) using design B, Fig. 1(b), was used for bio-imaging experiments. Fixed MCC13 cells were imaged sequentially for the red (660 nm) and green (561 nm) wavelengths. To image the plasma membrane stain, 0.3 mW laser power at 660 nm was measured on the back aperture of the objective lens used for coupling light into the waveguide chip. After consideration of the different loss contributions from coupling, bending and propagation, the guided power at the imaging region was roughly estimated to be in the order of 4-10 μW. Similarly, the microtubules were imaged using 5 mW of the 488 nm laser at the back aperture, leaving roughly around 0.5-1 μW of this wavelength at the imaging region. Given the high refractive index material, we estimate that around 10% of the guided power is available in the evanescent field. For each channel, 100 images were acquired with an integration time of 10 ms. An average of these images was used to further improve the image contrast, which can be seen in Figs. 6(a)-6(d). The position of the waveguide edges is indicated with white dashes in Figs. 6(a)-6(b), and zoomed regions indicated by white squares are shown in Figs. 6(c)-6(d). The evanescent field excitation of the waveguide gives high optical sectioning, generating images with high contrast and low background. The effects of shadows stemming from waveguide imperfections are minimal, but can be barely seen towards the right side of Fig. 6(a).

For live cell imaging, the HTR-8 cells were seeded and grown on the Si_3N_4 chip. The chip seeded with cells was placed inside the incubator for 48 hours. Live HTR-8 cells were imaged within 30 minutes after staining was completed. Input power of 60 mW of 488 nm laser was used at the back aperture of the coupling objective lens, which leaves around 15-30 μW guided power at the imaging region. A stack of images was acquired under continuous illumination for 3.6 minutes with 100 ms exposure time. The resulting movie, shown at Fig. 7 and Visualization 5, indicates a healthy environment for cell movement on the waveguide surface. Slight photobleaching was observed corresponding to around 25% decrease of the fluorescence intensity after 3.6 minutes of continuous illumination.

Optics EXPRESS

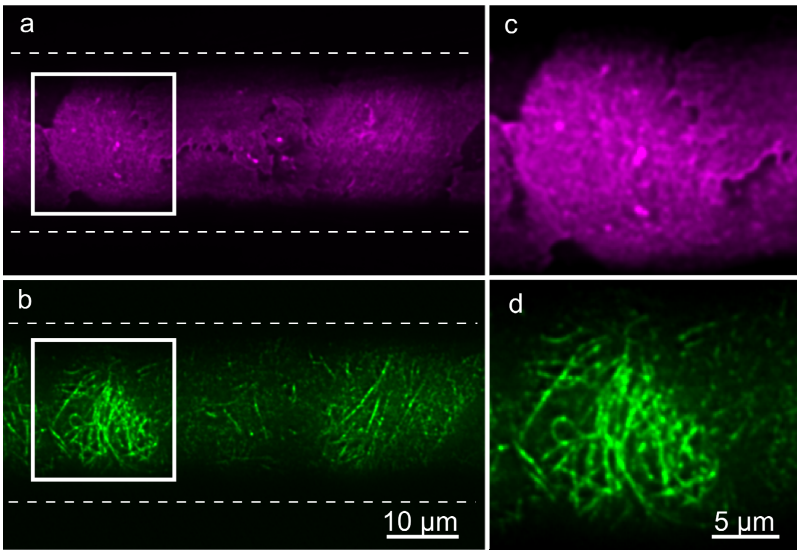

Fig. 6. a), b) MCC13 cells stained for plasma membrane (CellMask deep red) and tubulin (Alexa 488 anti-Tubulin), fluorescence excited through a 25 µm wide waveguide. The cells are distributed homogeneously on the chip, the center of the waveguide being indicated with dotted lines. c), d) are the regions indicated with a white box in a) and b). The cells are evenly illuminated at this position on the waveguide.

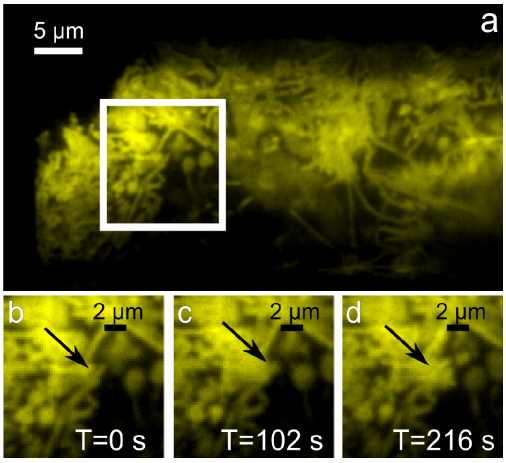

Fig. 7. HTR-8 cells stained for plasma membrane and kept alive in live-cell imaging media during the measurement. a) A frame from the movie (Visualization 5) shows several cells clustered together on the 25 µm wide waveguide. b) to d) Movement in the cell membrane can be seen over 3.6 minutes.

4. Conclusion and discussion

In this work we have systematically studied, developed and characterized a Si_3N_4 waveguide platform for bio-imaging applications. The fabrication of the Si_3N_4 platform is compatible with standard CMOS fabrication pilot lines. The high refractive index of the Si_3N_4 waveguide platform was exploited to generate a high intensity in the evanescent field by fabricating thin waveguides (150 nm). It was shown that Si_3N_4 waveguides provide biocompatible substrates where live cells can be grown and continuously imaged with low photo-toxicity, similar to the conventional glass cover slip approach.

Simulations backed up by experimental results studied the waveguide geometry to provide uniform illumination over wider widths (25 µm). A narrow (1.5 µm) and shallow rib

Optics EXPRESS

waveguide (4 nm) was adiabatically tapered to a wider width (25 μm) at the imaging region. To ensure single mode behavior at the imaging area, bend geometry was used. As higher order modes have much higher bend losses than the fundamental mode, it was demonstrated by bending the waveguide that higher order modes can be filtered out ensuring uniform illumination over wide waveguides (25 μm) at all studied wavelengths (488, 561 and 660 nm). In order to provide a uniform excitation, single mode waveguides are not always sufficient. Waveguide imperfections, dust particles, or other highly scattering or absorbing elements interfering with the guided mode may appear in the images as dark band shadows. The fabrication steps can be further optimized to reduce such artifacts. This effect is less prominent if the objects interfering the guided mode offer a less refractive index contrast, e.g., cells as shown in this work.

Propagation losses were measured for straight and bend sections, being low at longer wavelengths but showing a strong increase towards shorter wavelengths (488 nm). The propagation loss of less than 1 db/cm at 660 nm while it is around 10 db/cm at 488 nm. The high propagation losses at 488 nm seem to correlate with stronger auto-fluorescence at 488 nm wavelengths. Future optimization of the fabrication steps to reduce the auto-fluorescence at 488 nm will be carried out.

To fully exploit the capabilities of chip-based microscopy to provide large field of view TIRF illumination, future work will focus on extending the waveguide geometry laterally even further to accommodate uniform TIRF illumination suitable for imaging with low NA objectives. This will open up the possibility to study enormous populations of cells in TIRF mode in real-time enabling high-throughput TIRF imaging. Development of on-chip TIRF microscopy is also flexible towards implementations with other integrated systems, such as microfluidics and on-chip sensing, particle tracking and trapping and super-resolution microscopy.

Funding

European Research Council, project number 336716.

Acknowledgments

Authors acknowledge Martin Ingvaldsen for the code at scattering analysis and Rajwinder Singh for the assistance with sample preparations. This work has made use of the Spanish ICTS Network MICRONANOFABS partially supported by MEINCOM.